High-density equation of state for a two-dimensional Lennard-Jones solid

Kaihang Shi, Kai Gu, Yifan Shen, Deepti Srivastava, Erik E. Santiso, and Keith E. Gubbins

Citation: The Journal of Chemical Physics **148**, 174505 (2018); doi: 10.1063/1.5029488
View online: https://doi.org/10.1063/1.5029488
View Table of Contents: http://aip.scitation.org/toc/jcp/148/17
Published by the American Institute of Physics

PHYSICS TODAY
WHITEPAPERS

ADVANCED LIGHT CURE ADHESIVES

Take a closer look at what these environmentally friendly adhesive systems can do

READ NOW

PRESENTED BY
MASTERBOND
ADHESIVES | SEALANTS | COATINGS

High-density equation of state for a two-dimensional Lennard-Jones solid

Kaihang Shi,[1,a)] Kai Gu,[2,a)] Yifan Shen,[2] Deepti Srivastava,[1] Erik E. Santiso,[1,b)] and Keith E. Gubbins[1,b)]
[1]*Department of Chemical and Biomolecular Engineering, North Carolina State University, Raleigh, North Carolina 27606, USA*
[2]*Department of Chemistry, Zhejiang University, Hangzhou 310027, China*

(Received 14 March 2018; accepted 19 April 2018; published online 7 May 2018)

We present a new equation of state for a two-dimensional Lennard-Jones (2D LJ-EOS) solid at high densities, $\rho^*_{2D} \geq 0.9$. The new 2D LJ-EOS is of analytic form, consisting of a zero-temperature contribution and vibrational contributions up to and including the second anharmonic term. A detailed analysis of all contributing terms is performed. Comparisons between the 2D LJ-EOS and Monte Carlo simulation results show that the 2D LJ-EOS is very accurate over a wide range of temperatures in the high-density region. A criterion to find the temperature range over which the 2D LJ-EOS is applicable at a certain density is derived. We also demonstrate an application of the equation of state to predict an effective tangential pressure for the adsorbed contact layer near the wall in a slit-pore system. Tangential pressures predicted by this "2D-route" are found to be in qualitative agreement with those found by the more traditional virial route of Irving and Kirkwood. *Published by AIP Publishing.*
https://doi.org/10.1063/1.5029488

I. INTRODUCTION

Atomically thin two-dimensional (2D) systems are of interest because of their unique property behavior, being decisively different from that of three-dimensional systems. These marked differences arise because of the greatly reduced phase space available in 2D and the consequent reduction in the number of possible microstates, coordination number, entropy, and shielding of the molecules (for a schematic classical interpretation, see Fig. 1). Differences in thermodynamic behavior and in the phase diagram for Lennard-Jones (LJ) molecules due to the reduction from 3D to 2D have received much study.[1–7] The gas-liquid coexistence region of the diagram is much reduced, and the critical point occurs at a reduced temperature of $T^*_c \sim 0.5$ for 2D,[4] compared to $T^*_c \sim 1.3$ for 3D,[8,9] a result of the greatly diminished phase space in 2D. Here $T^*_c = k_B T_c/\varepsilon$. Moreover, the melting transition in 2D systems occurs by a different mechanism than that in 3D. According to the Kosterlitz-Thouless-Nelson-Halperin-Young theory,[10–13] the solid first undergoes a transition to a hexatic phase, having quasi-long-range orientational, but short-range positional, order, followed by a second transition to an isotropic fluid having both short-range orientational and positional orders. This metastable hexatic phase has been observed in the melting in 2D LJ systems.[14] Large-scale Monte Carlo (MC) simulation results were also reported to support the two-stage melting scenario in 2D LJ systems where the solid to a hexatic fluid (solid-hexatic) transition and a hexatic fluid to an isotropic liquid (hexatic-liquid) transition are both continuous phase transitions.[15] For hard disk systems, it was recently reported that the hexatic-liquid transition is of first order.[16,17] Two-dimensional systems have also proved of interest as a model for physical adsorption on planar solid substrates and in slit-shaped pores. Thus, the gas-liquid coexistence curve for a monolayer of LJ molecules on the planar graphite surface was found to be very close to that for the strictly 2D LJ fluid.[18]

Two-dimensional solid crystals occupy an important place in structural biology and medicine. Thus, some proteins readily self-assemble to form two-dimensional crystals on supported lipid bilayers, and 2D nucleation is one of the mechanisms by which 3D crystals grow.[19,20] Two-dimensional arrays also play a prominent role in DNA nano-technology.[21–23] Finally, we note the recent and intense interest in two-dimensional solid inorganic materials, starting with the preparation of graphene[24] and now expanded to include nearly 1000 two-dimensional materials that have either been synthesized or have been predicted to be possible.[25–27] In these covalently bonded 2D materials, the interest is primarily in their electronic, photonic, and magnetic properties, which reflect the increased quantum effects due to the reduction in phase space for 2D systems.

Several attempts have been made to develop a two-dimensional equation of state (EOS) for the LJ fluid, in part because the LJ fluid is a convenient reference fluid for more complicated systems. Henderson[28] developed an equation of state for two-dimensional Lennard-Jones fluids using the Barker-Henderson perturbation theory. An empirical term accounting for the higher-order expansion terms was added to the second-order theory, and the final semi-empirical 2D equation of state agreed very well with the simulation results. Reddy and O'Shea[29] fitted the equation of state for two-dimensional Lennard-Jones fluids to a modified

[a)]K. Shi and K. Gu contributed equally to this work.
[b)]Authors to whom correspondence should be addressed: eesantis@ncsu.edu and keg@ncsu.edu

	3D	2D	1D
Image	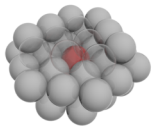	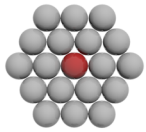	
Phase Space	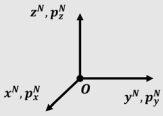	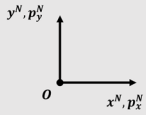	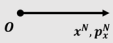
Coordination Number	12	6	2
Number of States, Ω	n^3	n^2	n
Entropy, $S/(k_B \ln n)$	3	2	1
Configurational Energy, $U_c/(N\varepsilon_{sw})$	-6	-3	-1

FIG. 1. A thermodynamicist's view of reduced dimensionality. For illustrative purposes, we employ a 3D face-centered cubic lattice. Reducing the number of dimensions from 3D to 2D to 1D causes large decreases in the available phase space, coordination number, number of possible microstates, Ω (n is the number of microstates per degree of freedom), entropy, $S = k_B \ln \Omega$ (k_B is the Boltzmann constant), and configurational energy (N is the number of molecules; molecules only interact with their nearest neighbors with a square-well potential having a potential well depth of ε_{sw}). Here Ω and S are values for a single energy level.

Benedict-Webb-Rubin (MBWR) equation. The 33 parameters in the equation were fitted to the pressure and energy data from the virial equation of state and to Monte Carlo simulations. The resulting equation of state offers a uniformly high-quality fit for pressure and energy for reduced temperatures and densities in the range $0.45 \le T^* \le 5$, $0.01 \le \rho^*_{2D} \le 0.80$ ($T^* = k_B T/\varepsilon$, $\rho^*_{2D} = N\sigma^2/S$, where k_B is the Boltzmann constant, N is the number of molecules, and S is the area; see Sec. II for the definition of ε and σ); the accuracy of the equation depends on the reliability of the critical constants. Freezing of the 2D LJ fluid to solid usually occurs at densities in the range $0.75 < \rho^*_{2D} < 0.9$, the exact value depending on the temperature.[1,5] The equations of state for a two-dimensional electrolyte[30] and for two-dimensional hard spheres[31–34] have also been reported.

Recently, Srivastava *et al.*[35] reported a molecular simulation study for a LJ adsorbate in a graphite slit pore, for cases where the interaction of the adsorbate molecules with the carbon walls is strong, corresponding to weak chemisorption. They showed that the adsorbed contact layer next to the graphene surface behaves like a two-dimensional solid with hexagonal close-packed structure and that the tangential pressures were very high near the wall, >10 GPa (hundreds of thousands of bar) and even higher in a few cases. Very high tangential pressure in the contact layer has also been reported in previous studies[36,37] for weaker adsorbate-wall interactions, in the range 1–6 GPa near the carbon walls; these adsorbed layers were also quasi-two dimensional in their structure. In these systems, the very strong attractive force field from the carbon walls causes the adsorbate molecules to pack tightly on the surface, and strong compression of these layers occurs in the xy plane, parallel to the walls, leading to these high tangential pressures. These quasi-2D adsorbed layers have very high 2D densities and have been observed to be in the range $0.9 \le \rho^*_{2D} \le 1.27$ for the weakly chemisorbing systems studied by Srivastava *et al.*[35] Thus the 2D density in such adsorbed films can be up to 70% higher than the density of the solid at the melting point, far beyond the densities considered in the earlier equations of state. To the best of our knowledge, there is no such two-dimensional equation of state for the Lennard-Jones system specifically constructed for such high-density systems ($\rho^*_{2D} \ge 0.9$).

In this work, we present a new theoretically based 2D Lennard-Jones equation of state (2D LJ-EOS) for the hexagonal close-packed 2D crystal structure. The extension to other packing structures is straightforward. Two-dimensional Monte Carlo simulations are performed to verify the validity of our 2D LJ-EOS. We also demonstrate one of the applications of this 2D LJ-EOS by using it to predict the effective tangential pressure of the adsorbed layers in several slit-pore systems.

II. TWO-DIMENSIONAL LENNARD-JONES EQUATION OF STATE

In this section, we derive the two-dimensional Lennard-Jones equation of state (2D LJ-EOS) for the hexagonal close-packed crystal phase. The intermolecular interactions are modeled as the 12-6 Lennard-Jones (LJ) potential,

$$u(r) = 4\varepsilon\left[\left(\frac{\sigma}{r}\right)^{12} - \left(\frac{\sigma}{r}\right)^{6}\right], \tag{1}$$

where ε is the LJ energy parameter and σ is the LJ atomic diameter. The 2D LJ-EOS expresses the 2D reduced pressure, $P^*_{2D} = P_{2D}\sigma^2/\varepsilon$, in terms of the reduced temperature, $T^* = k_B T/\varepsilon$, and 2D density, $\rho^*_{2D} = \rho_{2D}\sigma^2 = (N/S)\sigma^2$. The 2D pressure, P_{2D}, is the force per unit length acting on a line normal to the directions of the force and has units of Newton/meter. It is related to the Helmholtz free energy, A, by $P_{2D} = -(\partial A/\partial S)_{T,N}$.

The 2D LJ equation of state derived in this section has a rigorous theoretical basis and is composed of two parts: the contribution from the behavior of the solid at 0 K, when the molecules are at rest on their lattice sites, and the contribution from the vibrations of the particles, which must be included at finite temperatures. The contribution to the energy due to

the vibrations is obtained using a Taylor expansion about the zero-temperature state in powers of the displacement of the molecules from their lattice sites, keeping contributions up to the second anharmonic term.

A. Pressure at zero temperature

At zero temperature, we assume a perfect hexagonal packing of the molecules. This structure has the largest packing fraction, $\eta = \rho_{2D}\pi r_0^2/4 = \sqrt{3}\pi/6$, among all possible two-dimensional packing structures. Thus

$$\rho_{2D}^*\left(r_0^*\right)^2 = \rho_{2D} r_0^2 = \frac{2}{\sqrt{3}} \Rightarrow r_0^* = \left(\frac{2}{\sqrt{3}\rho_{2D}^*}\right)^{1/2}, \tag{2}$$

where $r_0^* = r_0/\sigma$ is the separation between particles in units of σ. In this case, all particles are at their equilibrium positions, forming a perfect hexagonal two-dimensional crystal. The position of the particle is given by vector $\mathbf{r}_{i,j}^*$ in units of σ,

$$\mathbf{r}_{i,j}^* = r_0^*\left[\left(i + \frac{1}{2}j\right)\mathbf{e}_x + \frac{\sqrt{3}}{2}j\mathbf{e}_y\right], \tag{3}$$

where i and j are integers, representing the generalized coordinates in the hexagonal structure. We assume that the intermolecular forces are pair-wise additive. The total specific configurational energy is

$$U_0^* = \lim_{L,M\to\infty} \frac{2}{(L+1)(M+1)} \sum_{i,j=0,0}^{L,M} \sum_{\substack{l,m=0,0 \\ l,m\neq i,j}}^{L,M} \left[\left(\frac{1}{\left\|\mathbf{r}_{i,j}^* - \mathbf{r}_{l,m}^*\right\|}\right)^{12} - \left(\frac{1}{\left\|\mathbf{r}_{i,j}^* - \mathbf{r}_{l,m}^*\right\|}\right)^{6}\right], \tag{4}$$

where $U_0^* = U_0/\varepsilon$ and coefficient 1/2 is included here to avoid double counting. We notice that by using Eqs. (2) and (3), Eq. (4) can be rewritten as

$$\begin{aligned} U_0^* &= \lim_{L,M\to\infty} \frac{2}{(L+1)(M+1)} \\ &\quad \times \sum_{i,j=0,0}^{L,M} \sum_{\substack{l,m=0,0 \\ l,m\neq i,j}}^{L,M} \left[\frac{1}{\left(r_0^*\sqrt{\alpha_{ijlm}}\right)^{12}} - \frac{1}{\left(r_0^*\sqrt{\alpha_{ijlm}}\right)^{6}}\right] \\ &= \lim_{L,M\to\infty} \frac{1}{(L+1)(M+1)} \left[\frac{27}{32}\left(\rho_{2D}^*\right)^6 \sum_{i,j=0,0}^{L,M} \sum_{\substack{l,m=0,0 \\ l,m\neq i,j}}^{L,M} \frac{1}{\alpha_{ijlm}^6} \right. \\ &\quad \left. - \frac{3^{3/2}}{4}\left(\rho_{2D}^*\right)^3 \sum_{i,j=0,0}^{L,M} \sum_{\substack{l,m=0,0 \\ l,m\neq i,j}}^{L,M} \frac{1}{\alpha_{ijlm}^3}\right], \end{aligned} \tag{5}$$

TABLE I. The temperature- and density-independent expressions for the κ_i coefficients, where $\alpha_{ijlm} = [(i-l)^2 + (i-l)(j-m) + (j-m)^2]$ for κ_1 and κ_2. Numerical values are available in Table II.

i	κ_i	i	κ_i
1	$\frac{81}{16}\lim_{L,M\to\infty}\frac{1}{(L+1)(M+1)}\sum_{i,j=0,0}^{L,M}\sum_{\substack{l,m=0,0\\l,m\neq i,j}}^{L,M}\frac{1}{\alpha_{ijlm}^6}$	10	$243\sqrt{3}\lim_{L,M\to\infty}\sum_{\substack{i,j=-L,-M\\i,j\neq 0,0}}^{L,M}\frac{14i^4+28i^3j+12i^2j^2-2ij^3-j^4}{\left(i^2+j^2+ij\right)^7}$
2	$\frac{3^{5/2}}{4}\lim_{L,M\to\infty}\frac{1}{(L+1)(M+1)}\sum_{i,j=0,0}^{L,M}\sum_{\substack{l,m=0,0\\l,m\neq i,j}}^{L,M}\frac{1}{\alpha_{ijlm}^3}$	11	$\frac{5103\sqrt{3}}{4}\lim_{L,M\to\infty}\sum_{\substack{i,j=-L,-M\\i,j\neq 0,0}}^{L,M}\frac{j(2i+j)\left(10i^2+10ij+j^2\right)}{\left(i^2+j^2+ij\right)^{10}}$
3	$\frac{3^{9/2}}{16}\lim_{L,M\to\infty}\sum_{\substack{i,j=-L,-M\\i,j\neq 0,0}}^{L,M}\frac{5j^2+26i^2+26ij}{\left(i^2+j^2+ij\right)^8}$	12	$3645\lim_{L,M\to\infty}\sum_{\substack{i,j=-L,-M\\i,j\neq 0,0}}^{L,M}\frac{ij(2i+j)(i+j)}{\left(i^2+j^2+ij\right)^7}$
4	$\frac{27}{2}\lim_{L,M\to\infty}\sum_{\substack{i,j=-L,-M\\i,j\neq 0,0}}^{L,M}\frac{j^2+7i^2+7ij}{\left(i^2+j^2+ij\right)^5}$	13	$\frac{5103}{8}\lim_{L,M\to\infty}\sum_{\substack{i,j=-L,-M\\i,j\neq 0,0}}^{L,M}\frac{-5i^4-10i^3j+57i^2j^2+62ij^3+13j^4}{\left(i^2+j^2+ij\right)^{10}}$
5	$\frac{3^{9/2}}{16}\lim_{L,M\to\infty}\sum_{\substack{i,j=-L,-M\\i,j\neq 0,0}}^{L,M}\frac{19j^2-2i^2-2ij}{\left(i^2+j^2+ij\right)^8}$	14	$243\sqrt{3}\lim_{L,M\to\infty}\sum_{\substack{i,j=-L,-M\\i,j\neq 0,0}}^{L,M}\frac{-2i^4-4i^3j+14i^2j^2+16ij^3+3j^4}{\left(i^2+j^2+ij\right)^7}$
6	$\frac{27}{2}\lim_{L,M\to\infty}\sum_{\substack{i,j=-L,-M\\i,j\neq 0,0}}^{L,M}\frac{5j^2-i^2-ij}{\left(i^2+j^2+ij\right)^5}$	15	$\frac{5103\sqrt{3}}{4}\lim_{L,M\to\infty}\sum_{\substack{i,j=-L,-M\\i,j\neq 0,0}}^{L,M}\frac{j(2i+j)\left(-2i^2-2ij+7j^2\right)}{\left(i^2+j^2+ij\right)^{10}}$
7	$\frac{1701}{16}\lim_{L,M\to\infty}\sum_{\substack{i,j=-L,-M\\i,j\neq 0,0}}^{L,M}\frac{j^2+2ij}{\left(i^2+j^2+ij\right)^8}$	16	$1215\lim_{L,M\to\infty}\sum_{\substack{i,j=-L,-M\\i,j\neq 0,0}}^{L,M}\frac{j(2i+j)(i+2j)(j-i)}{\left(i^2+j^2+ij\right)^7}$
8	$3^{7/2}\lim_{L,M\to\infty}\sum_{\substack{i,j=-L,-M\\i,j\neq 0,0}}^{L,M}\frac{j^2+2ij}{\left(i^2+j^2+ij\right)^5}$	17	$\frac{5103}{8}\lim_{L,M\to\infty}\sum_{\substack{i,j=-L,-M\\i,j\neq 0,0}}^{L,M}\frac{i^4+2i^3j-21i^2j^2-22ij^3+31j^4}{\left(i^2+j^2+ij\right)^{10}}$
9	$\frac{5103}{8}\lim_{L,M\to\infty}\sum_{\substack{i,j=-L,-M\\i,j\neq 0,0}}^{L,M}\frac{65i^4+130i^3j+75i^2j^2+10ij^3-j^4}{\left(i^2+j^2+ij\right)^{10}}$	18	$81\sqrt{3}\lim_{L,M\to\infty}\sum_{\substack{i,j=-L,-M\\i,j\neq 0,0}}^{L,M}\frac{2i^4+4i^3j-24i^2j^2-26ij^3+17j^4}{\left(i^2+j^2+ij\right)^7}$

TABLE II. Numerical values of the parameter κ_i. Parameters required to evaluate the new two-dimensional Lennard-Jones equation of state [Eq. (31)] are marked in bold.

i	κ_i	i	κ_i
1	**30.424 683 010 328 2**	10	10 154.249 752 770 6
2	**24.847 539 283 054 7**	11	0
3	**631.661 435 732 493**	12	0
4	**247.231 027 231 675**	13	**26 795.252 184 019 0**
5	631.661 435 732 493	14	**3 384.749 917 590 16**
6	247.231 027 231 675	15	0
7	0	16	0
8	0	17	80 385.756 552 057 2
9	80 385.756 552 057 2	18	10 154.249 752 770 6

where $\alpha_{ijlm} = [(i-l)^2 + (i-l)(j-m) + (j-m)^2]$. From the basic thermodynamic relations, we can get the pressure at zero temperature by

$$P^*_{2D,T=0} = \left(\rho^*_{2D}\right)^2 \left(\frac{\partial U^*_0}{\partial \rho^*_{2D}}\right). \tag{6}$$

By substituting Eq. (5) into Eq. (6), we can obtain the zero-temperature contribution to the 2D pressure as a function of the system density,

$$P^*_{2D,T=0} = \kappa_1 \left(\rho^*_{2D}\right)^7 - \kappa_2 \left(\rho^*_{2D}\right)^4, \tag{7}$$

where κ_1 and κ_2 are constants and their expressions are listed in Table I. The values of κ_1 and κ_2 can be obtained from the numerical calculations and their values converge very rapidly with increasing L and M. The numerical values of κ_1 and κ_2 are summarized in Table II to high accuracy.

B. Pressure at finite temperature

To account for the effect of vibrations at non-zero temperatures, we expand about the zero-temperature result in powers of the displacement of the molecules from their equilibrium lattice sites. Thus, for each term in this expansion, a given LJ molecule vibrates under the potential generated by all the others at their average (equilibrium) positions. We can thus calculate the vibration energy as a sum of such oscillators. For the Lennard-Jones particles, the background mean-field energy is

$$U^*(\mathbf{r}^*) = 4 \lim_{L,M\to\infty} \sum_{\substack{i,j=-L,-M \\ i,j\neq 0,0}}^{L,M} \left[\frac{1}{\left\|\mathbf{r}^* - \mathbf{r}^*_{i,j}\right\|^{12}} - \frac{1}{\left\|\mathbf{r}^* - \mathbf{r}^*_{i,j}\right\|^{6}} \right], \tag{8}$$

where $\mathbf{r}^*$ is the reduced position of the central particle and $\mathbf{r}^*_{i,j}$ is the equilibrium lattice position of other particles. Let function $f_{i,j}$ be

$$f_{i,j} = \frac{1}{\left\|\mathbf{r}^* - \mathbf{r}^*_{i,j}\right\|^{12}} - \frac{1}{\left\|\mathbf{r}^* - \mathbf{r}^*_{i,j}\right\|^{6}}. \tag{9}$$

For temperatures that are not too high, the displacement of the particles from their lattice sites will be small, and the contribution from vibrations can be described using a simple harmonic oscillator term (the first non-vanishing term in the expansion). To get the harmonic force constant for the central particle, we need to calculate the 2nd-order gradient of the background potential field, i.e., the Hessian matrix,

$$\begin{aligned}
\mathbf{H} = \nabla_{\mathbf{r}^*}\nabla_{\mathbf{r}^*} U^*(\mathbf{r}^*) &= 4 \lim_{L,M\to\infty} \sum_{\substack{i,j=-L,-M \\ i,j\neq 0,0}}^{L,M} \begin{bmatrix} \frac{\partial^2 f_{i,j}}{\partial x^* \partial x^*} & \frac{\partial^2 f_{i,j}}{\partial x^* \partial y^*} \\ \frac{\partial^2 f_{i,j}}{\partial y^* \partial x^*} & \frac{\partial^2 f_{i,j}}{\partial y^* \partial y^*} \end{bmatrix} \\
&= 96 \lim_{L,M\to\infty} \sum_{\substack{i,j=-L,-M \\ i,j\neq 0,0}}^{L,M} \left[7\frac{1}{\left\|\mathbf{r}^* - \mathbf{r}^*_{i,j}\right\|^{16}} - 2\frac{1}{\left\|\mathbf{r}^* - \mathbf{r}^*_{i,j}\right\|^{10}} \right] \times \begin{bmatrix} \left(x^* - x^*_{i,j}\right)^2 & \left(x^* - x^*_{i,j}\right)\left(y^* - y^*_{i,j}\right) \\ \left(x^* - x^*_{i,j}\right)\left(y^* - y^*_{i,j}\right) & \left(y^* - y^*_{i,j}\right)^2 \end{bmatrix} \\
&\quad + 24 \lim_{L,M\to\infty} \sum_{\substack{i,j=-L,-M \\ i,j\neq 0,0}}^{L,M} \left[-2\frac{1}{\left\|\mathbf{r}^* - \mathbf{r}^*_{i,j}\right\|^{14}} + \frac{1}{\left\|\mathbf{r}^* - \mathbf{r}^*_{i,j}\right\|^{8}} \right] \begin{bmatrix} 1 & 0 \\ 0 & 1 \end{bmatrix},
\end{aligned} \tag{10}$$

where x^* and y^* are the reduced Cartesian coordinates of the central particle. From Eqs. (2) and (3), we can easily relate $\mathbf{r}^*_{i,j}$ (i.e., $x^*_{i,j}$ and $y^*_{i,j}$) to the density ρ^*_{2D} through

$$x^*_{i,j} = \left(\frac{2}{\sqrt{3}\rho^*_{2D}}\right)^{1/2} \left(i + \frac{j}{2}\right), \qquad y^*_{i,j} = \left(\frac{\sqrt{3}}{2\rho^*_{2D}}\right)^{1/2} j. \tag{11}$$

If we evaluate the Hessian matrix at $\mathbf{r}^* = 0$ and rewrite $x^*_{i,j}$ and $y^*_{i,j}$ in terms of the density, then Eq. (10) becomes

$$\mathbf{H}_0 = 96 \lim_{L,M\to\infty} \sum_{\substack{i,j=-L,-M \\ i,j\neq 0,0}}^{L,M} \left[7\frac{1}{\left\|\mathbf{r}^*_{i,j}\right\|^{16}} - 2\frac{1}{\left\|\mathbf{r}^*_{i,j}\right\|^{10}} \right] \times \begin{bmatrix} \left(x^*_{i,j}\right)^2 & x^*_{i,j}y^*_{i,j} \\ x^*_{i,j}y^*_{i,j} & \left(y^*_{i,j}\right)^2 \end{bmatrix} + 24 \lim_{L,M\to\infty} \sum_{\substack{i,j=-L,-M \\ i,j\neq 0,0}}^{L,M} \left[-2\frac{1}{\left\|\mathbf{r}^*_{i,j}\right\|^{14}} + \frac{1}{\left\|\mathbf{r}^*_{i,j}\right\|^{8}} \right] \begin{bmatrix} 1 & 0 \\ 0 & 1 \end{bmatrix}$$
$$= \begin{bmatrix} \alpha & \gamma \\ \gamma & \beta \end{bmatrix}, \tag{12}$$

where

$$\begin{aligned} \alpha &= \lim_{L,M\to\infty} \sum_{\substack{i,j=-L,-M \\ i,j\neq 0,0}}^{L,M} \left\{ 96\left[7\frac{1}{\left\|\mathbf{r}^*_{i,j}\right\|^{16}} - 2\frac{1}{\left\|\mathbf{r}^*_{i,j}\right\|^{10}} \right]\left(x^*_{i,j}\right)^2 + 24\left[-2\frac{1}{\left\|\mathbf{r}^*_{i,j}\right\|^{14}} + \frac{1}{\left\|\mathbf{r}^*_{i,j}\right\|^{8}} \right] \right\} \\ &= 96 \lim_{L,M\to\infty} \sum_{\substack{i,j=-L,-M \\ i,j\neq 0,0}}^{L,M} \left[7\frac{81\left(\rho^*_{2D}\right)^8}{256(i^2+ij+j^2)^8} - \frac{3^{5/2}\left(\rho^*_{2D}\right)^5}{16(i^2+ij+j^2)^5} \right]\left(\frac{2}{\sqrt{3}\rho^*_{2D}}\right)\left(i+\frac{j}{2}\right)^2 \\ &\quad + 24 \lim_{L,M\to\infty} \sum_{\substack{i,j=-L,-M \\ i,j\neq 0,0}}^{L,M} \left[-\frac{3^{7/2}\left(\rho^*_{2D}\right)^7}{64(i^2+ij+j^2)^7} + \frac{9\left(\rho^*_{2D}\right)^4}{16(i^2+ij+j^2)^4} \right] \\ &= \kappa_3\left(\rho^*_{2D}\right)^7 - \kappa_4\left(\rho^*_{2D}\right)^4 \end{aligned} \tag{13}$$

and similarly

$$\beta = \kappa_5\left(\rho^*_{2D}\right)^7 - \kappa_6\left(\rho^*_{2D}\right)^4, \tag{14}$$

$$\gamma = \kappa_7\left(\rho^*_{2D}\right)^7 - \kappa_8\left(\rho^*_{2D}\right)^4, \tag{15}$$

where the expressions for κ_i ($i = 3, 4, \ldots, 8$) are summarized in Table I. The numerical values of those coefficients are listed in Table II. We found that $\alpha \approx \beta$ and $\gamma \approx 0$ (see Appendix A). Therefore, the Hessian matrix evaluated at $\mathbf{r}^* = 0$ in Eq. (12) can be simplified to

$$\mathbf{H}_0 = \alpha\begin{pmatrix} 1 & 0 \\ 0 & 1 \end{pmatrix}. \tag{16}$$

The harmonic force constants are the eigenvalues of the Hessian matrix. Hence, the reduced harmonic energy U^*_{har} of the central particle in terms of the polar coordinates can then be written as

$$U^*_{har} = \frac{\alpha}{2}(r^*)^2, \tag{17}$$

where $U^*_{har} = U_{har}/\varepsilon$ and the radial coordinate r^* represents the distance of the central particle from its lattice site ($\mathbf{r}^* = 0$) in units of σ. So, the partition function of a single harmonic oscillator is

$$\begin{aligned} q_{har} &= \frac{1}{\Lambda^2}\int_{\mathbf{R}^2} \exp\left(-\frac{U^*_{har}}{T^*}\right) \mathrm{d}^2\mathbf{r} \\ &= \frac{1}{\Lambda^2}\int_0^{2\pi} d\theta \int_0^{\infty} \exp\left[-\frac{\alpha(r^*)^2}{2T^*}\right] r^* \mathrm{d}r^* \\ &= \frac{2\pi T^*}{\Lambda^2\alpha}, \end{aligned} \tag{18}$$

where $\Lambda = (h^2/2\pi m k_B T)^{1/2}$ is the de Broglie wavelength and the integration is over the whole 2D phase space. Consequently, the total harmonic partition function of the system is

$$Q_{har} = q^N_{har}. \tag{19}$$

Once the total partition function is known, other thermodynamic properties can be readily obtained. From Eqs. (13), (18), and (19), the 2D pressure contributed from the harmonic vibrations of all particles in the system can be calculated as

$$\begin{aligned} P^*_{har} &= -T^*\left(\rho^*_{2D}\right)^2\left(\frac{\partial \ln Q^{1/N}_{har}}{\partial \rho^*_{2D}}\right)_T \\ &= \frac{T^*\left(\rho^*_{2D}\right)^2}{\alpha}\left(\frac{\partial \alpha}{\partial \rho^*_{2D}}\right)_T \\ &= \frac{7\kappa_3\left(\rho^*_{2D}\right)^4 - 4\kappa_4\rho^*_{2D}}{\kappa_3\left(\rho^*_{2D}\right)^3 - \kappa_4}T^*. \end{aligned} \tag{20}$$

Combining Eqs. (7) and (20), an approximate, but simple, equation of state can be obtained for the harmonic crystal, where terms higher than quadratic ones are negligible at low enough temperatures.[38] At higher temperatures, our Monte Carlo simulations indicate that only including this harmonic contribution to the pressure is insufficient for an accurate description of the 2D system (see Fig. 2 and further discussions in Sec. III B). To extend our treatment to higher temperatures, we need to include one or more higher-order anharmonic terms in the expansion.

To evaluate the first anharmonic term, the third order gradient of the background mean-field potential is needed, which is a 3rd order tensor $\mathbf{I}$. We note that if the central particle is

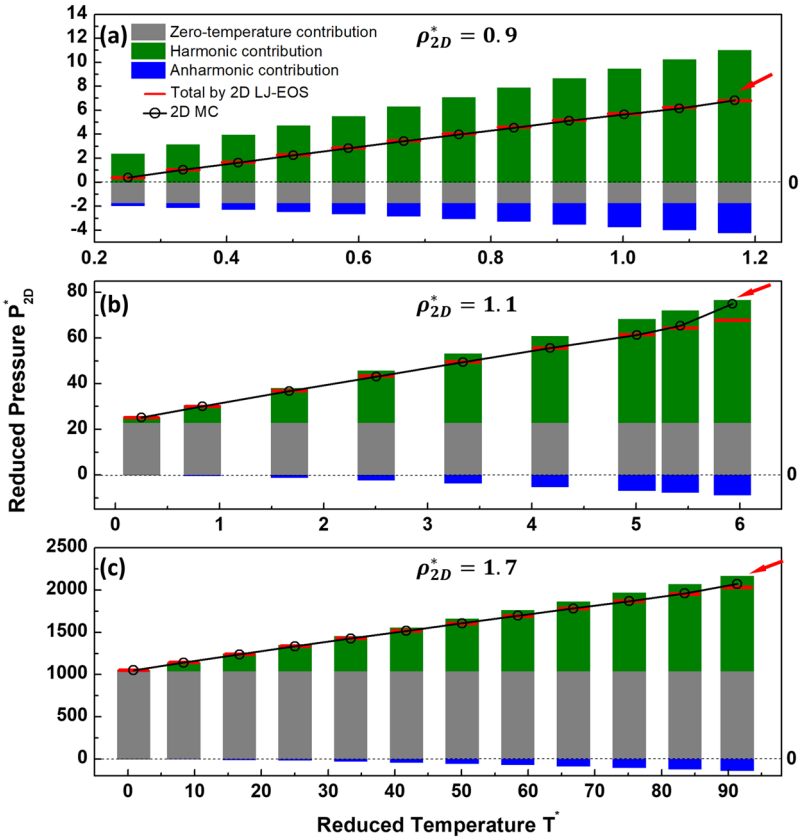

FIG. 2. Decompositions of the 2D LJ-EOS into zero-temperature contribution (gray column), harmonic contribution (green column), and anharmonic contribution (blue column) in a pressure-temperature (P-T) diagram at different densities. (a) $\rho^*_{2D} = 0.9$. (b) $\rho^*_{2D} = 1.1$. (c) $\rho^*_{2D} = 1.7$. The total 2D pressures predicted by the 2D LJ-EOS (red bar) are compared with exact 2D MC simulation results (open circle). Systems where a defective crystal/liquid is simulated are marked by red arrows. Lines are drawn to guide the eye.

evaluated at the reference position, $\mathbf{r}^* = 0$, this 3rd order tensor $\mathbf{I_0}$ will be zero due to the symmetry of the hexagonal structure, hence leading to a trivial anharmonic term (see Appendix B). Therefore, we calculate the second anharmonic term, for which we need the 4th order gradient tensor $\mathbf{G}$, evaluated at $\mathbf{r}^* = 0$,

$$\mathbf{G_0} = \nabla_{\mathbf{r}^*}\nabla_{\mathbf{r}^*}\nabla_{\mathbf{r}^*}\nabla_{\mathbf{r}^*}U^*(\mathbf{r}^* = 0)$$
$$= 4\lim_{L,M\to\infty}\sum_{\substack{i,j=-L,-M\\ i,j\neq 0,0}}^{L,M}\left[\begin{array}{cccc}
\frac{\partial^4 f_{i,j}}{\partial x^*\partial x^*\partial x^*\partial x^*} & \frac{\partial^4 f_{i,j}}{\partial x^*\partial y^*\partial x^*\partial x^*} & \frac{\partial^4 f_{i,j}}{\partial x^*\partial x^*\partial y^*\partial x^*} & \frac{\partial^4 f_{i,j}}{\partial x^*\partial y^*\partial y^*\partial x^*} \\
\frac{\partial^4 f_{i,j}}{\partial y^*\partial x^*\partial x^*\partial x^*} & \frac{\partial^4 f_{i,j}}{\partial y^*\partial y^*\partial x^*\partial x^*} & \frac{\partial^4 f_{i,j}}{\partial y^*\partial x^*\partial y^*\partial x^*} & \frac{\partial^4 f_{i,j}}{\partial y^*\partial y^*\partial y^*\partial x^*} \\
\frac{\partial^4 f_{i,j}}{\partial x^*\partial x^*\partial x^*\partial y^*} & \frac{\partial^4 f_{i,j}}{\partial x^*\partial y^*\partial x^*\partial y^*} & \frac{\partial^4 f_{i,j}}{\partial x^*\partial x^*\partial y^*\partial y^*} & \frac{\partial^4 f_{i,j}}{\partial x^*\partial y^*\partial y^*\partial y^*} \\
\frac{\partial^4 f_{i,j}}{\partial y^*\partial x^*\partial x^*\partial y^*} & \frac{\partial^4 f_{i,j}}{\partial y^*\partial y^*\partial x^*\partial y^*} & \frac{\partial^4 f_{i,j}}{\partial y^*\partial x^*\partial y^*\partial y^*} & \frac{\partial^4 f_{i,j}}{\partial y^*\partial y^*\partial y^*\partial y^*}
\end{array}\right]\Bigg|_{\mathbf{r}^*=0}$$
$$= \begin{bmatrix} a & b & b & c \\ b & c & c & d \\ b & c & c & d \\ c & d & d & e \end{bmatrix}, \tag{21}$$

where $\mathbf{G_0}$ is written as a (4×4) matrix, but actually it is a 4th-order tensor $(2 \times 2 \times 2 \times 2)$. By doing some mathematical manipulations similar to Eq. (12), each component in this (4×4) matrix can be written in terms of the system density,

$$a = \kappa_9\left(\rho^*_{2D}\right)^8 - \kappa_{10}\left(\rho^*_{2D}\right)^5, \tag{22}$$
$$b = \kappa_{11}\left(\rho^*_{2D}\right)^8 - \kappa_{12}\left(\rho^*_{2D}\right)^5, \tag{23}$$
$$c = \kappa_{13}\left(\rho^*_{2D}\right)^8 - \kappa_{14}\left(\rho^*_{2D}\right)^5, \tag{24}$$

$$d = \kappa_{15}\left(\rho_{2D}^*\right)^8 - \kappa_{16}\left(\rho_{2D}^*\right)^5, \tag{25}$$

$$e = \kappa_{17}\left(\rho_{2D}^*\right)^8 - \kappa_{18}\left(\rho_{2D}^*\right)^5. \tag{26}$$

The analytical expressions for κ_i ($i = 9, 10, \ldots, 18$) are given in Table I. The numerical values of κ_i are listed in Table II. Similarly, we found that $a = e \approx 3c$ and $b = -d \approx 0$. By using these relations, the total reduced vibrational energy U_{vib}^*, including both harmonic and anharmonic contributions, can be written in polar coordinates as

$$\begin{aligned} U_{vib}^* &= \frac{c}{8}\left[(x^*)^2 + (y^*)^2\right]^2 + \frac{\alpha}{2}\left[(x^*)^2 + (y^*)^2\right] \\ &= \frac{c}{8}(r^*)^4 + \frac{\alpha}{2}(r^*)^2. \end{aligned} \tag{27}$$

The corresponding vibrational partition function of a single oscillator is

$$\begin{aligned} q_{vib} &= \frac{1}{\Lambda^2}\int_{\mathbf{R}^2} \exp\left(-\frac{U_{vib}^*}{T^*}\right) \mathrm{d}^2\mathbf{r} \\ &= \frac{\exp\left[\alpha^2/(2cT^*)\right]}{\Lambda^2}\int_0^{2\pi} d\theta \int_0^{+\infty} \exp\left\{-\frac{c}{8T^*}\left[(r^*)^2 + \frac{2\alpha}{c}\right]^2\right\} r^* \mathrm{d}r^* \\ &= \sqrt{\frac{2\pi^3 T^*}{\Lambda^4 c}}\exp\left(\frac{\alpha^2}{2cT^*}\right) erfc\left(\frac{\alpha}{\sqrt{2cT^*}}\right). \end{aligned} \tag{28}$$

Therefore, the total vibrational partition function of the system is given by

$$Q_{vib} = q_{vib}^N. \tag{29}$$

The vibrational contribution to the 2D pressure can be derived from the total vibrational partition function, Eq. (29); by using Eqs. (13), (24), (28), and (29), we get

$$\begin{aligned} P_{2D,vib}^* &= -T^*\left(\rho_{2D}^*\right)^2\left(\frac{\partial \ln Q_{vib}^{1/N}}{\partial \rho_{2D}^*}\right)_T \\ &= \frac{\left(\rho_{2D}^*\right)^2\alpha}{2c^2}\left(\alpha\frac{\partial c}{\partial \rho_{2D}^*} - 2c\frac{\partial \alpha}{\partial \rho_{2D}^*}\right) + \frac{\left(\rho_{2D}^*\right)^2}{2c}\frac{\partial c}{\partial \rho_{2D}^*}T^* - \frac{\left(\rho_{2D}^*\right)^2}{\sqrt{2\pi c^3}}\left(\alpha\frac{\partial c}{\partial \rho_{2D}^*} - 2c\frac{\partial \alpha}{\partial \rho_{2D}^*}\right)\frac{e^{\frac{-\alpha^2}{2cT^*}}\sqrt{T^*}}{erfc\left(\frac{\alpha}{\sqrt{2cT^*}}\right)} \\ &= \frac{-6\kappa_{13}\kappa_3^2\left(\rho_{2D}^*\right)^{13} + \left(9\kappa_3^2\kappa_{14} + 6\kappa_3\kappa_4\kappa_{13}\right)\left(\rho_{2D}^*\right)^{10} - 12\kappa_3\kappa_4\kappa_{14}\left(\rho_{2D}^*\right)^7 + 3\kappa_{14}\kappa_4^2\left(\rho_{2D}^*\right)^4}{2\kappa_{13}^2\left(\rho_{2D}^*\right)^6 - 4\kappa_{13}\kappa_{14}\left(\rho_{2D}^*\right)^3 + 2\kappa_{14}^2} + \frac{8\kappa_{13}\left(\rho_{2D}^*\right)^4 - 5\kappa_{14}\left(\rho_{2D}^*\right)}{2\kappa_{13}\left(\rho_{2D}^*\right)^3 - 2\kappa_{14}}T^* \\ &\quad + \sqrt{\frac{T^*\rho_{2D}^*}{2\pi\left[\kappa_{13}\left(\rho_{2D}^*\right)^3 - \kappa_{14}\right]^3}}\left[6\kappa_3\kappa_{13}\left(\rho_{2D}^*\right)^8 - 9\kappa_3\kappa_{14}\left(\rho_{2D}^*\right)^5 + 3\kappa_4\kappa_{14}\left(\rho_{2D}^*\right)^2\right] \\ &\quad \times\frac{\exp\left\{-\left(\rho_{2D}^*\right)^3\left[\kappa_3\left(\rho_{2D}^*\right)^3 - \kappa_4\right]^2 \Big/ \left[2T^*\kappa_{13}\left(\rho_{2D}^*\right)^3 - 2T^*\kappa_{14}\right]\right\}}{erfc\left\{\left[\kappa_3\left(\rho_{2D}^*\right)^5 - \kappa_4\left(\rho_{2D}^*\right)^2\right] \Big/ \sqrt{2T^*\left[\kappa_{13}\left(\rho_{2D}^*\right)^4 - \kappa_{14}\left(\rho_{2D}^*\right)\right]}\right\}}. \end{aligned} \tag{30}$$

Equation (30) is a non-linear function in terms of the temperature. Combining Eqs. (7) and (30), an expression to calculate the total 2D pressure can be obtained as a sum of the zero-temperature contribution and that from the particle vibrations, including both harmonic and anharmonic vibrational terms,

$$P_{2D}^* = P_{2D,T=0}^* + P_{2D,vib}^*. \tag{31}$$

The parameters needed to evaluate Eq. (31) are marked in bold in Table II. The pressure calculated by Eq. (31) includes both kinetic and configurational contributions. From Eqs. (5) and (29), we can also readily derive the Helmholtz free energy of the 2D system, which is given by

$$\begin{aligned} A^* &= A_0^* + A_{vib}^* \\ &= NU_0^* - T^* \ln Q_{vib}, \end{aligned} \tag{32}$$

where $A^* = A/\varepsilon$ and subscript "0" and "vib" denote the zero-temperature contribution and vibrational contribution, respectively.

III. VERIFICATION OF THE NEW 2D LJ-EOS

A. Simulation details

Two-dimensional canonical Monte Carlo (2D MC) simulations of Lennard-Jones particles were performed to verify the validity of the new 2D LJ-EOS derived in Sec. II. The number of particles (N), area ($S = L_xL_y$), and temperature (T) were fixed in the simulation. The box lengths were chosen to allow the system to form a hexagonal structure. Periodic boundary conditions were applied in the x and y directions. At least 200 spherical Lennard-Jones argon particles were used in each simulation, with potential parameters of $\sigma = 3.405$ Å and $\varepsilon/k_B = 119.8$ K. The cut-off radius for the 12-6 Lennard-Jones potential was $r_c = 5\sigma$, and a tail correction to the configurational energy was added,

$$U_{tail} = \frac{4\pi\varepsilon N^2}{S}\left[\frac{\sigma^2}{10}\left(\frac{\sigma}{r_c}\right)^{10} - \frac{\sigma^2}{4}\left(\frac{\sigma}{r_c}\right)^4\right]. \tag{33}$$

The 2D pressure of the system was calculated by the area perturbation method using the central finite-difference approximation,[39]

$$\beta P_{2D} = \frac{1}{2|\xi|S} \ln \frac{\left\langle (1+\xi)^N \exp(-\beta \Delta U^+) \right\rangle}{\left\langle (1-|\xi|)^N \exp(-\beta \Delta U^-) \right\rangle}, \quad (34)$$

where $\beta = (k_B T)^{-1}$; the relative change in the area is denoted by $\xi \equiv \Delta S/S$, the value of which has been discussed in Ref. 39. The energy change $\Delta U^+ = U(S + \Delta S) - U(S)$ is associated with the increase in area, and $\Delta U^- = U(S - |\Delta S|) - U(S)$ is the energy change associated with the decrease in area. The angular bracket denotes the ensemble average. We note that at these high densities it is very easy for the system to become trapped in a local minimum, and it will take a very long time for the system to escape from that local minimum and reach the global minimum. This issue can be avoided by the use of a perfect hexagonal structure as the initial configuration. The equilibrium stage of the simulation consisted of 10×10^6 configurations, and the statistics were sampled from the following production stage, consisting of a further 10×10^6 configurations. We divided the production stage into 10 blocks, and the standard deviations of these 10 blocks were computed.

B. Results and discussion

In derivation of the vibrational contribution to the 2D pressure in Sec. II B, we made a mean-field approximation that the central particle vibrates under the potential generated by all the others at their equilibrium lattice positions so that the total vibrational energy is a sum of such independent oscillators. That approximation enables us to reduce a many-body problem to a simple one-body problem, but neglects the collective vibrations that occur in the real solid. To better understand the validity of this mean-field approximation in the derivation of the 2D LJ-EOS, we decomposed the total 2D pressure into each contributing component, i.e., zero-temperature contribution, harmonic contribution, and anharmonic contribution; we show these contributions in Fig. 2. Low density ($\rho^*_{2D} = 0.9$), intermediate density ($\rho^*_{2D} = 1.1$), and ultrahigh density ($\rho^*_{2D} = 1.7$) systems are all considered. For the low-density system, in Fig. 2(a), we can see that both the zero-temperature and anharmonic terms are negative. Since the zero-temperature term [Eq. (7)] is only a function of density, its value remains constant with temperature. For the harmonic term, because the increase of temperature enhances the vibrational kinetic energy of the lattice sites, its value linearly increases with the temperature [see Eq. (20)]. The total 2D pressures predicted by the 2D LJ-EOS are also compared with the exact 2D MC results in Fig. 2. In addition to the zero-temperature and harmonic contributions, we can see that the quantitative agreement between the theoretical and simulation results would not be reached without including the negative anharmonic term. The anharmonic contributions become more and more important with increasing temperature and are comparable to the zero-temperature contributions in the case of $\rho^*_{2D} = 0.9$. If we further look at the intermediate-density case ($\rho^*_{2D} = 1.1$) and ultrahigh-density case ($\rho^*_{2D} = 1.7$) in Figs. 2(b) and 2(c), the systems are much denser, and the zero-temperature term becomes positive. In these two cases, at low temperatures, the zero-temperature term is the largest contribution to the total pressure and possible errors in the vibrational term are negligible. Again, as the temperature goes up, the harmonic term contributes more to the pressure and the inclusion of the negative anharmonic term ensures the quantitative agreement between the 2D LJ-EOS the 2D MC results. However, the anharmonic term becomes less important compared to the other two contributing terms when the system density increases. We note that at high enough temperatures (marked by red arrows in Fig. 2), the theoretical results by the 2D LJ-EOS start deviating from the exact 2D MC results. For those state points, we observed either a defective crystal or liquid phase in the 2D MC simulations. We note that the 2D LJ-EOS presented here shows excellent agreement with the MC results over the recommended range of densities and temperatures for which the EOS is expected to hold, as seen in Figs. 2–5. The EOS neglects anharmonic terms higher than the second and also neglects collective lattice vibrations. Contributions from higher anharmonic terms appear to be negligible, provided that the upper temperature limits prescribed below [see Eq. (36)] are respected. It follows from this and the good agreement with the MC results that the contributions from collective vibrations will also be very small in the range of densities and temperatures for which the EOS is constructed. Including the latter effects in our EOS would result in considerable additional complexity, with minimal benefit in accuracy.

The isotherms for argon calculated from 2D MC and the 2D LJ-EOS are compared in the P^*_{2D} - ρ^*_{2D} diagram shown in Fig. 3. The relative deviations of the pressure between the two methods are also plotted in Fig. 4. From Figs. 3 and 4, we can see that large fluctuations in the deviation occur in the low-density region, while in the high-density region, there is almost zero deviation between the two methods. This is because there is more free space in the low-density system

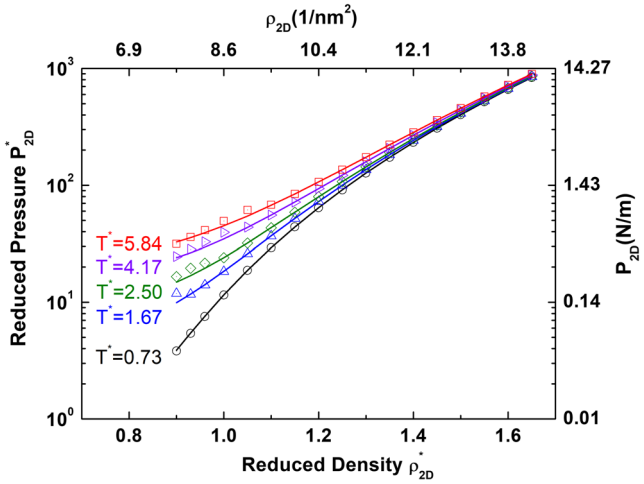

FIG. 3. Isotherms for the pressure-density diagram for the two-dimensional LJ system at high density from 2D MC (symbols) and 2D LJ-EOS (solid lines) at reduced temperature of 0.73 (87.3 K), 1.67 (200 K), 2.50 (300 K), 4.17 (500 K), and 5.84 (700 K). Real units are for LJ argon (with $\sigma = 3.405$ Å and $\varepsilon/k_B = 119.8$ K). Error bars (standard deviation) are always smaller than the size of the symbol.

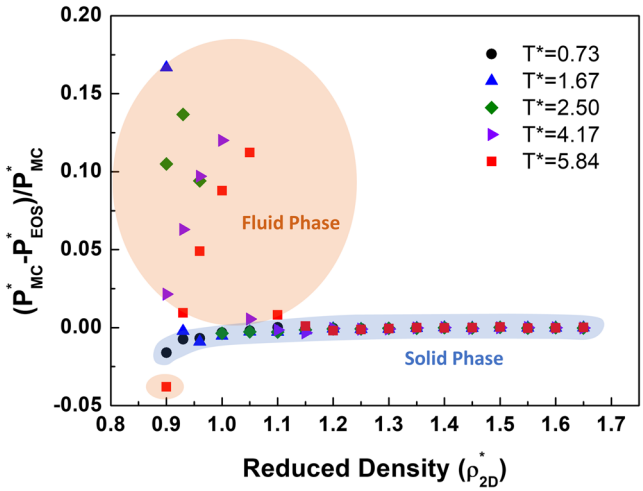

FIG. 4. The relative deviation plot for pressure at different temperatures, where P^*_{MC} is the 2D MC simulation result and P^*_{EOS} is the 2D LJ-EOS calculation, both of which are taken from Fig. 3. Points corresponding to fluid phase (orange region) or solid phase (blue region) are marked in the plot. See text for details.

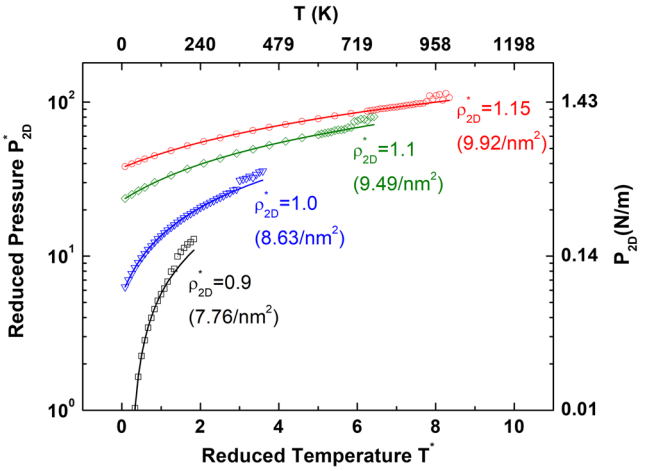

FIG. 5. Pressure-temperature (P-T) diagram for the two-dimensional LJ system at fixed densities from 2D MC (symbols) and 2D LJ-EOS (solid lines). Real units are for LJ argon (with σ = 3.405 Å and ε/k_B = 119.8 K). Error bars (standard deviation) are always smaller than the size of the symbol.

than in the high-density system. With increasing temperature, particles with random thermal motion about their equilibrium positions[1] move more freely in the low-density system than those in the high-density system. Thus, the hexagonal structure at low density is more easily disrupted. In Fig. 4, we have marked the points where the fluid phase or solid phase is simulated. Due to the small simulation system used in this work, we cannot distinguish between the liquid phase and any hexatic phase that could be present. Thus, some state points marked in the fluid phase in Fig. 4 could possibly be in the metastable hexatic phase. We can expect that, because of the limited thermal motion of atoms in the high-density region, once the crystal is formed at a given temperature, our 2D LJ-EOS will remain accurate at even higher density, beyond the highest reduced density shown in the plot. An extended pressure-temperature (P-T) diagram at different densities is shown in Fig. 5. We can see that for each fixed-density curve, when temperature is higher than an upper limiting value, which is defined as T_{lim}, our 2D LJ-EOS results start deviating from the exact 2D MC results. A typical configuration for the 2D LJ argon system at a high temperature above T_{lim} is shown in Fig. 6(a); according to the phase diagram of the 2D Lennard-Jones fluid,[1] the system is not in the solid phase at this state condition, and the hexagonal lattice assumption made in the 2D LJ-EOS is no longer valid. However, when we decrease the temperature, the system re-enters the solid phase, and the hexagonal crystal is the most thermodynamically stable structure [Fig. 6(b)]. The simulation results and 2D LJ-EOS calculations are in good agreement again with almost zero relative deviation.

In Fig. 5, we have defined an upper temperature limit, T_{lim}, above which the 2D LJ-EOS calculations start deviating significantly from the 2D MC results. From a molecular perspective, when $T > T_{\text{lim}}$ at a given density, the random thermal motion of the central particle is so intense that the Maclaurin expansion made in the derivation of the 2D LJ-EOS up to the fourth order term is no longer enough. To use this 2D LJ-EOS, we must therefore find out the temperature range over which the EOS is accurate for each specific density, i.e., the value of T_{lim} as a function of ρ_{2D}. In the 2D system, the average kinetic energy of a particle is T^* in reduced units. Because the total energy of an oscillating system is conserved, the kinetic energy at the reduced limiting temperature T^*_{lim} can be written as

$$T^*_{\text{lim}} = U^*_{vib}\left(r^*_{\text{lim}}\right), \tag{35}$$

where U^*_{vib} given by Eq. (27) is a function of r^*_{lim}. Here, r^*_{lim} is the largest distance of the central particle away from its equilibrium position to maintain the validity of the 2D LJ-EOS. For the lower density range ($0.9 \le \rho^*_{2D} < 1.0$), due to the statistical uncertainties in the simulation, the lowest relative deviation

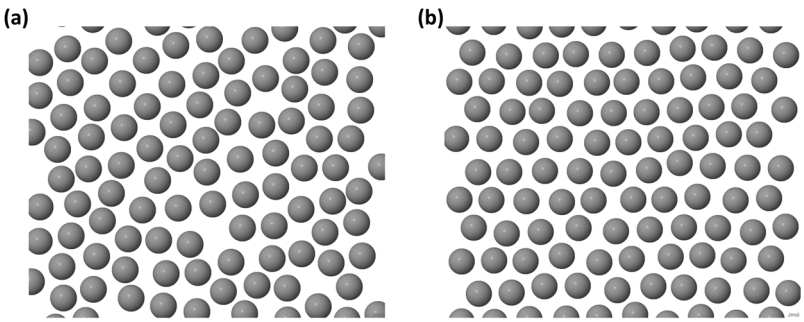

FIG. 6. Configurations of the 2D Lennard-Jones argon system at (a) ρ^*_{2D} = 1.0, T^* = 4.17 (500 K) and (b) ρ^*_{2D} = 1.0, T^* = 1.67 (200 K). When ρ^*_{2D} = 1.0, the upper limiting temperature T_{lim} ~ 313 K. The argon molecules are drawn to the reduced scale for clarity.

between the MC and EOS methods is around 1%, while for the higher density range ($\rho^*_{2D} \geq 1.0$), the lowest relative deviation is almost zero. Therefore, we can find this upper temperature limit T^*_{lim} from our MC simulation results for a certain density by observing the lowest temperature point at which the relative deviation between the 2D LJ-EOS calculation and the simulation result is larger than 5% (for $0.9 \leq \rho^*_{2D} < 1.0$) and 1.5% (for $\rho^*_{2D} \geq 1.0$). By means of a trial and error process, we find that $r^*_{\text{lim}} \approx r^*_0/10$, where r^*_0 is the separation between lattice sites in a perfect hexagonal crystal, and can be related to the reduced density through Eq. (2). From Eqs. (2), (13), (24), and (27), Eq. (35) can be written as

$$\begin{aligned} T^*_{\text{lim}} &\approx U^*_{vib}\left(r^*_0/10\right) \\ &= \left(\frac{\kappa_{13}}{60\,000} + \frac{\kappa_3}{100\sqrt{3}}\right)\left(\rho^*_{2D}\right)^6 \\ &\quad - \left(\frac{\kappa_{14}}{60\,000} + \frac{\kappa_4}{100\sqrt{3}}\right)\left(\rho^*_{2D}\right)^3, \end{aligned} \tag{36}$$

where κ_3, κ_4, κ_{13}, and κ_{14} are constants whose values are listed in Table II. The T^*_{lim} derived from Eq. (36) are compared with the T^*_{lim} found in 2D MC simulations in Fig. 7. The upper temperature limit from Eq. (36) is in generally good agreement with that found in Monte Carlo simulations for the higher densities. For the lower densities, the predicted T^*_{lim} from Eq. (36) are consistently lower than those found in the simulations, which implies that Eq. (36) provides a conservative criterion to predict the T^*_{lim}. Moreover, we found that this T_{lim} is a rough estimate of the onset temperature of the melting of the solid. Due to the hexatic phase between the solid and liquid phase that may occur in two-dimensional Lennard-Jones systems,[14] this T_{lim} could lie between the melting temperature T_m (transition temperature from a solid to a hexatic fluid) and the transition temperature T_i from a hexatic fluid to an isotropic liquid. For example, when $\rho^*_{2D} = 0.873$, $T^*_m = 0.61 < T^*_{\text{lim}} \approx 0.825 < T^*_i \approx 0.92$.[15] Thus, by using Eq. (36), a workable temperature range (i.e., $T^* < T^*_{\text{lim}}$) for the new 2D LJ-EOS can easily be determined at a reduced density of interest. For example, when $\rho^*_{2D} = 1.0$, Eq. (36) gives $T^*_{\text{lim}} \approx 2.61$, which corresponds to the real temperature of 313 K for the LJ argon case in Fig. 6.

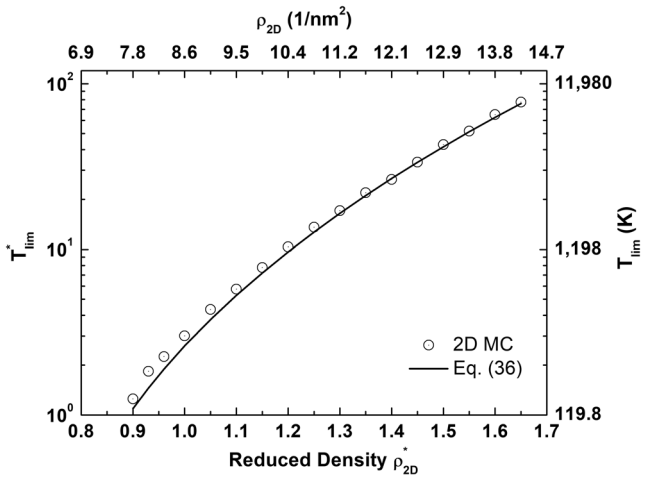

FIG. 7. The upper temperature limit T^*_{lim} found from Eq. (36) (solid line) and from 2D MC simulations (symbols). Real units are for LJ argon (with σ = 3.405 Å and ε/k_B = 119.8 K).

IV. APPLICATION OF 2D LJ-EOS TO THE ADSORBED CONTACT LAYER IN SLIT PORE SYSTEMS

Here we illustrate one use of the high-density equation of state, namely, a new route to estimate the effective tangential pressure in a thin adsorbed film on a planar solid surface. There is a great deal of evidence from both the experiment and molecular simulation that strong compression can occur for molecules adsorbed on a wetting solid surface.[35] Thus, for strongly attractive surfaces such as carbons, the pressure in the film parallel to the surface can be enhanced by 4-5 orders of magnitude over the pressure in the bulk phase in equilibrium with the adsorbed film.[37,40]

Near to the surface of the substrate the film is highly inhomogeneous so that the pressure **P** is a second-order tensor,[41–43] having components $P_{\alpha\beta}$, the force per unit area in the β-direction acting on an element of surface pointing in (i.e., normal to) the α-direction. The statistical mechanical expression for this pressure[42,43] consists of the sum of a kinetic term (ideal gas term) due to the molecular motion, $\rho(z)kT$, where $\rho(z)$ is the 3D number density, N/V, at distance z from the surface of the substrate, and a configurational term which is an average of the intermolecular forces in the β-direction per unit area acting on the element of surface. In the examples to be discussed here, it is the configurational part of the pressure that is dominant, comprising 80%-90% or more of the total pressure. If the system is not under strain, the off-diagonal elements of the pressure tensor are zero, leaving only the three diagonal elements, P_{xx},P_{yy},P_{zz}. Here we take z to be the direction normal to the surface so that the surface lies in the xy plane. From the symmetry of the planar surface, $P_{xx} = P_{yy}$ so that there are two independent pressures: the tangential pressure $P_T = P_{xx} = P_{yy}$ parallel to the substrate surface and the pressure acting normal to the surface, $P_N = P_{zz}$. Finally, we note that the condition of hydrostatic equilibrium states that there is no net transfer of momentum between the adsorbed film and the bulk phase with which it is in equilibrium, and this places some restrictions on the behavior of the pressure components; in the absence of any external field, this condition is expressed as

$$\nabla \cdot \mathbf{P} = 0. \tag{37}$$

A difficulty arises when considering the pressure in an adsorbed film that is inhomogeneous on the range of the intermolecular forces. Because the forces are due to intermolecular interactions between pairs, triplets, etc. of molecules, there is no unique way to assign the contribution of these forces to a particular point in space, **r**. Thus, there is no unique definition of the pressure tensor at the nanoscale. For the special case of a planar surface, the normal pressure is well defined. Thus, Eq. (37) for the planar surface leads to $\partial P_N/\partial z = 0$ so that the normal pressure is constant and independent of the distance z from the surface; for a single planar surface, far enough from the surface, the normal pressure must equal the pressure in the bulk phase that is in equilibrium with the adsorbed film, and this pressure is well defined and a scalar. However, the

tangential pressure is not uniquely defined, and its value will depend on the path chosen between the centers of two nearby molecules. This difficulty was recognized by Irving and Kirkwood (IK),[41] who defined the path to be a straight line joining the two molecules; if this line crosses the element of surface, the pair force contributes to the pressure. Other definitions of the path between two molecules have been used, including that of Harasima (H),[44] and give somewhat different numerical values for the tangential pressure;[45,46] for gas-liquid surfaces, molecular simulation results show that the IK and H definitions yield tangential pressures that differ significantly, but these differences are less than 10%.[45,46] Many studies have used the Irving-Kirkwood (IK) operational definition to calculate the pressure tensor at position $\mathbf{r}$, which can be calculated in molecular simulations as[35]

$$\mathbf{P}_{IK}(\mathbf{r}) = \rho(\mathbf{r})k_BT\mathbf{1} - \frac{1}{2}\left\langle \sum_{i\neq j}^{N} \frac{\mathbf{r}_{ij}\mathbf{r}_{ij}}{r_{ij}} \frac{du(r_{ij})}{dr_{ij}} \times \int_0^1 d\lambda\, \delta(\mathbf{r}_i - \mathbf{r} + \lambda\mathbf{r}_{ij}) \right\rangle, \tag{38}$$

where $\mathbf{1}$ is the second-order unit tensor. The second term on the right of this equation is the ensemble average of the virial, and Eq. (38) is known as the virial, or mechanical, route to the pressure.

Molecular simulation results for slit-shaped pores[35–37] show that for adsorbates that wet the pore walls the adsorbed layers of molecules very near to the wall are quasi-two-dimensional. An example taken from the work of Srivastava *et al.*[35] is shown in Fig. 8(a) and displays the quasi-2D structure of the adsorbed layers, this being particularly pronounced for the contact layers next to the pore walls. These authors used a simplified pore model in which the adsorbate LJ molecules interact with the walls via a Steele (10,4,3) interaction,[47]

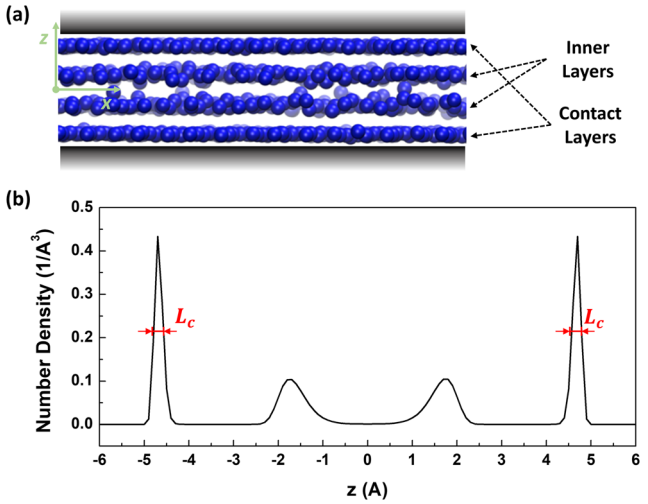

FIG. 8. Molecular simulation results for a LJ adsorbate (a) in a slit pore of width $H^* = H/\sigma_{aa} = 5.0$ and wetting parameter $\alpha_w = 10$. (a) Snapshot of the structure of the four adsorbed layers; (b) density profile of the four adsorbed layers in the z-direction. Here the density profile is symmetric about the center of the pore ($z = 0$) and the high-density peaks correspond to the contact layers next to the pore wall. The characteristic length, L_c, in Eq. (41) is marked in red in the figure. Adsorbate molecules are drawn at a reduced scale for clarity. (Reprinted with permission from D. Srivastava, E. E. Santiso, and K. E. Gubbins, Langmuir **33**, 11231 (2017). Copyright 2017 American Chemical Society.)

given by

$$u_{as}(z) = 2\pi\rho_s\sigma_{as}^2\varepsilon_{as}\Delta\left[\frac{2}{5}\left(\frac{\sigma_{as}}{z}\right)^{10} - \left(\frac{\sigma_{as}}{z}\right)^4 - \left(\frac{\sigma_{as}^4}{3\Delta(z+0.61\Delta)^3}\right)\right], \tag{39}$$

where z is the distance of the adsorbate molecule (a) from the solid surface (s), ρ_s is the number density of solid atoms in the wall, and Δ is the separation distance between layers of wall atoms, here taken to be carbon, the wall consisting of graphite. This equation is derived by summing up all the LJ interactions between a single adsorbate molecule and the carbon atoms in the substrate. With this model wall, it is possible to define a microscopic *wetting parameter*, α_w, as the ratio of the strength of interaction of an adsorbate molecule with the wall to the interaction between two adsorbate molecules,

$$\alpha_w = \frac{\text{Adsorbate - Wall Interaction}}{\text{Adsorbate - Adsorbate Interaction}} = \rho_s\sigma_{as}^2\Delta\left(\frac{\varepsilon_{as}}{\varepsilon_{aa}}\right). \tag{40}$$

A value of $\alpha_w = 0$ corresponds to complete non-wetting, while large values of α_w indicate strong wetting. In this pore model, there are two dimensionless parameters α_w and $H^* = H/\sigma_{aa}$ that characterize the pore.

The behavior of the contact layer of adsorbate molecules can be related to that of a strictly 2D reference film by projecting the center of mass positions of the molecules in the layer onto an xy plane (keeping the x and y values of each molecule fixed) drawn through the average of the actual center of mass positions in the z-direction. The two-dimensional density, $\rho_{2D} = N/S$, of these projected molecules in the layer can be read from the simulation results, and the ensemble average value of these 2D densities can then be used in the 2D LJ equation of state to determine the corresponding pressure, P_{2D}, of the 2D reference film. The tangential pressure in the slit pore is a three-dimensional pressure, having units of force per unit area; we take this pressure to be that due to the force in the y direction acting on an area element in the xz plane (i.e., pointing in the y-direction). By contrast, P_{2D} has units of force per unit length; it is the force in the y-direction acting on an element of length in the x-direction. We now define an effective tangential pressure in the slit pore, as calculated by this new 2D route, as

$$P_{T,2D} \equiv \frac{P_{2D}}{L_c}, \tag{41}$$

where L_c is a characteristic length in the z-direction. While P_{2D} is the 2D pressure in a homogeneous film and is well defined, L_c is not well defined, reflecting the fact that the tangential pressure in the 3D inhomogeneous system is not well defined. It seems reasonable to conclude that L_c should be related to the thickness of the adsorbed layer; for the contact layers shown in Fig. 8(b), this thickness is less than 1 Å. Here we choose L_c to be width of the density profile of the contact layer at half of its peak value, which is readily calculated from the simulation results [see Fig. 8(b)].

TABLE III. Comparison between the effective tangential pressure, $P_{T,2D}$, of Eq. (41), derived from the 2D LJ-EOS in this work, and the reported peak value[35] of the tangential pressure for the contact layer, $P_{T,IK}$, of Eq. (38), calculated from the Irving-Kirkwood (IK) virial route. Calculations are for LJ nitric oxide, NO, at a temperature of 140 K ($T^* = 1.12$) and a bulk phase pressure of 0.16 bar.[a] See text for further details.

	ρ^*_{2D}	P^*_{2D}	P_{2D}(N/m)	L^*_c	$P_{T,2D}$(GPa)	$P_{T,IK}$(GPa)	Deviation
$H = 3\sigma_{aa}, \alpha_w = 10$	1.00	14.4889	0.2486	0.07342	10.68	11.58	7.8%
$H = 3\sigma_{aa}, \alpha_w = 39$	1.16	50.9826	0.8748	0.05905	46.71	48.46	3.6%
$H = 5\sigma_{aa}, \alpha_w = 10$	1.02	17.0994	0.2934	0.06863	13.48	16.12	16.4%
$H = 5\sigma_{aa}, \alpha_w = 39$	1.27	108.216	1.8568	0.03511	166.7	224.5	25.7%

[a] $\rho^*_{2D} = N\sigma^2_{aa}/S$, $P^*_{2D} = P_{2D}\sigma^2_{aa}/\varepsilon_{aa}$, $L^*_c = L_c/\sigma_{aa}$, $T^* = k_BT/\varepsilon_{aa}$,
Deviation $= |P_{T,IK} - P_{T,2D}|/P_{T,IK}$.

In Table III, we show results for the effective tangential pressure calculated from the 2D route of Eq. (41) and compare these with the peak tangential pressures for the contact layer, $P_{T,IK}$, calculated from the IK virial route of Eq. (38), using the simulation data of Srivastava *et al.*[35] The data are for two pore widths, H^* of 3.0 and 5.0, and for two values of α_w, 10 and 39, corresponding to weak chemisorption of the adsorbate with the pore walls. The results given in Table III are for a temperature of 140 K ($T^* = 1.12$), which is well within the range of validity of the 2D LJ-EOS at the densities considered, as seen from Eq. (36) and Fig. 7. The reduced units in Table III are converted to real units by using the Lennard-Jones parameters for nitric oxide, NO, as used by Srivastava *et al.*;[35] $\sigma_{aa} = 0.317\,15$ nm, $\varepsilon_{aa}/k_B = 125.0$ K.

The results for the effective tangential pressures in Table III show qualitative agreement between the IK virial route and the 2D route. For the pore width of $H^* = 3$, the pore only contains two adsorbed layers, both of which are contact layers on the two opposing pore walls. These layers are close to two-dimensional in their structure, and the difference between the pressures given by the two routes is less than 10%. For the larger pores of $H^* = 5$, the difference in pressures from the two routes is larger, but still less than 30%. The deviations between these two routes are probably due to the arbitrary choice of the characteristic length, L_c.

V. CONCLUSION

In this study, we present the derivation of a new two-dimensional Lennard-Jones equation of state (2D LJ-EOS), which is specifically designed for the crystalline solid phase ($\rho^*_{2D} \geq 0.9$). The new 2D LJ-EOS is composed of two parts: the pressure at zero Kelvin and the vibrational contribution to the pressure at non-zero temperature. For the vibrational contribution, we include both the harmonic term and the second anharmonic term (the first anharmonic term is zero). Two-dimensional Monte Carlo (2D MC) simulations were carried out to test the validity of the 2D LJ-EOS. The simulation results show quantitative agreement with the 2D LJ-EOS calculations over a wide range of temperatures in the high-density region. Our 2D LJ-EOS neglects contributions from anharmonic terms of 3rd order and higher and also neglects collective lattice vibration effects. The excellent agreement of the EOS with the MC simulations suggests that any such effects are very small in the range of state conditions considered.

We also present an equation in terms of reduced density to find the upper temperature limit, T^*_{lim}, for the 2D LJ-EOS. When, for a given density, the working temperature is lower than T^*_{lim}, the 2D LJ-EOS can give a pressure value close to the exact 2D MC result with relative deviation within 5% for $0.9 \leq \rho^*_{2D} < 1.0$ and 1.5% for $\rho^*_{2D} \geq 1.0$. This T^*_{lim} was also found to be a rough estimate of the melting temperature for 2D LJ solid.

Following the validation of the accuracy of the 2D LJ-EOS and of the temperature and density range over which it is applicable, we have demonstrated its application to estimate the effective tangential pressure of the adsorbed contact layer in slit-pore systems. The value, $P_{T,2D}$, predicted by this new "2D route" agrees qualitatively with the peak tangential pressure values, $P_{T,IK}$, obtained via the virial Irving-Kirkwood route,[35] the deviation between the two routes being less than 10% for the smaller pore of width $H^* = 3$ and about 25% for the larger $H^* = 5$ pore. The inner adsorbed layers, farther from the pore walls, have a more diffuse structure than the contact layers [see Fig. 8(a)] so that the simple "2D route" used here is uncertain to give an accurate representation of the effective tangential pressure in these layers; however, a perturbation treatment about the 2D LJ system might offer a better representation. The new 2D LJ-EOS could also be extended to study adsorbed layers of mixtures by using the van der Waals 1-fluid theory.[48,49]

ACKNOWLEDGMENTS

The authors thank Professor Jerzy Bernholc and Professor George Jackson for helpful discussions, and an anonymous reviewer for several suggestions that improved our manuscript. This work was supported by the U.S. National Science Foundation under Grant No. CBET-1603851.

APPENDIX A: HESSIAN MATRIX FOR HARMONIC TERM

From Eqs. (12)–(15), we want to prove that $\alpha = \beta$ and $\gamma = 0$. That is,

$$\kappa_3 - \kappa_5 = \kappa_4 - \kappa_6 = \kappa_7 = \kappa_8 = 0. \tag{A1}$$

Using the expressions in Table I, we assume that the following four equations are correct:

$$\lambda_1 = \kappa_3 - \kappa_5 = \lim_{L,M\to\infty} \sum_{\substack{i,j=-L,-M \\ i,j\neq 0,0}}^{L,M} \frac{2i^2 - j^2 + 2ij}{\left(i^2 + j^2 + ij\right)^8} = 0, \tag{A2}$$

$$\lambda_2 = \kappa_4 - \kappa_6 = \lim_{L,M\to\infty} \sum_{\substack{i,j=-L,-M \\ i,j\neq 0,0}}^{L,M} \frac{2i^2 - j^2 + 2ij}{\left(i^2 + j^2 + ij\right)^5} = 0, \tag{A3}$$

$$\lambda_3 = \kappa_7 = \lim_{L,M\to\infty} \sum_{\substack{i,j=-L,-M \\ i,j\neq 0,0}}^{L,M} \frac{j^2 + 2ij}{\left(i^2 + j^2 + ij\right)^8} = 0, \tag{A4}$$

$$\lambda_4 = \kappa_8 = \lim_{L,M\to\infty} \sum_{\substack{i,j=-L,-M \\ i,j\neq 0,0}}^{L,M} \frac{j^2 + 2ij}{\left(i^2 + j^2 + ij\right)^5} = 0, \tag{A5}$$

where i and j are dummy variables and exchanging them will not affect the final limiting results. By replacing i with j and j with i, Eqs. (A2)–(A5) can also be equivalently written as

$$\lambda_1' = \lim_{L,M\to\infty} \sum_{\substack{i,j=-L,-M \\ i,j\neq 0,0}}^{L,M} \frac{2j^2 - i^2 + 2ij}{\left(i^2 + j^2 + ij\right)^8}, \tag{A6}$$

$$\lambda_2' = \lim_{L,M\to\infty} \sum_{\substack{i,j=-L,-M \\ i,j\neq 0,0}}^{L,M} \frac{2j^2 - i^2 + 2ij}{\left(i^2 + j^2 + ij\right)^5}, \tag{A7}$$

$$\lambda_3' = \lim_{L,M\to\infty} \sum_{\substack{i,j=-L,-M \\ i,j\neq 0,0}}^{L,M} \frac{i^2 + 2ij}{\left(i^2 + j^2 + ij\right)^8}, \tag{A8}$$

$$\lambda_4' = \lim_{L,M\to\infty} \sum_{\substack{i,j=-L,-M \\ i,j\neq 0,0}}^{L,M} \frac{i^2 + 2ij}{\left(i^2 + j^2 + ij\right)^5}, \tag{A9}$$

where $\lambda_i = \lambda_i'$ $(i = 1,2,3,4)$. Then we have

$$\lambda_i + \lambda_i' = \lim_{L,M\to\infty} \sum_{\substack{i,j=-L,-M \\ i,j\neq 0,0}}^{L,M} \frac{i^2 + j^2 + 4ij}{\left(i^2 + j^2 + ij\right)^8} = 0 \quad (\mathrm{i} = 1,3), \tag{A10}$$

$$\lambda_i + \lambda_i' = \lim_{L,M\to\infty} \sum_{\substack{i,j=-L,-M \\ i,j\neq 0,0}}^{L,M} \frac{i^2 + j^2 + 4ij}{\left(i^2 + j^2 + ij\right)^5} = 0 \quad (\mathrm{i} = 2,4). \tag{A11}$$

We further demonstrate that

$$\lambda_i + \lambda_i' = \lim_{L,M\to\infty} \sum_{\substack{i,j=-L,-M \\ i,j\neq 0,0}}^{L,M} \frac{i^2 + j^2 + 4ij}{\left(i^2 + j^2 + ij\right)^n} = 0, \tag{A12}$$

where n = 5 and 8. We numerically calculated the value of Eq. (A12), and found that its value converges very quickly to about -1E-16, which approximates the machine precision. Therefore, we can safely say that

$$\lambda_i + \lambda_i' \approx 0 \tag{A13}$$

because $\lambda_i = \lambda_i'$ $(i = 1,2,3,4)$, $\lambda_i \approx 0$. Consequently, we've numerically proved that $\alpha \approx \beta$ and $\gamma \approx 0$.

APPENDIX B: EVALUATION OF THIRD ORDER GRADIENT OF THE BACKGROUND ENERGY

The third order gradient of the background mean-field energy, evaluated at $\mathbf{r}^* = 0$, can be written as

$$\begin{aligned}
\mathbf{I_0} = \nabla_{\mathbf{r}^*}\nabla_{\mathbf{r}^*}\nabla_{\mathbf{r}^*}U^*(\mathbf{r}^* = 0) &= 4 \lim_{L,M\to\infty} \sum_{\substack{i,j=-L,-M \\ i,j\neq 0,0}}^{L,M} \left[\begin{array}{cccc} \frac{\partial^3 f_{i,j}}{\partial x^*\partial x^*\partial x^*} & \frac{\partial^3 f_{i,j}}{\partial y^*\partial x^*\partial x^*} & \frac{\partial^3 f_{i,j}}{\partial x^*\partial y^*\partial x^*} & \frac{\partial^3 f_{i,j}}{\partial y^*\partial y^*\partial x^*} \\ \frac{\partial^3 f_{i,j}}{\partial x^*\partial x^*\partial y^*} & \frac{\partial^3 f_{i,j}}{\partial y^*\partial x^*\partial y^*} & \frac{\partial^3 f_{i,j}}{\partial x^*\partial y^*\partial y^*} & \frac{\partial^3 f_{i,j}}{\partial y^*\partial y^*\partial y^*} \end{array}\right]\Bigg|_{\mathbf{r}^*=0} \\
&= 384 \lim_{L,M\to\infty} \sum_{\substack{i,j=-L,-M \\ i,j\neq 0,0}}^{L,M} \left[-28\frac{1}{\left\|\mathbf{r}_{i,j}^*\right\|^{18}} + 5\frac{1}{\left\|\mathbf{r}_{i,j}^*\right\|^{12}}\right] \left[\begin{array}{cccc} \left(x_{i,j}^*\right)^3 & \left(x_{i,j}^*\right)^2 y_{i,j}^* & \left(x_{i,j}^*\right)^2 y_{i,j}^* & x_{i,j}^*\left(y_{i,j}^*\right)^2 \\ \left(x_{i,j}^*\right)^2 y_{i,j}^* & x_{i,j}^*\left(y_{i,j}^*\right)^2 & x_{i,j}^*\left(y_{i,j}^*\right)^2 & \left(y_{i,j}^*\right)^3 \end{array}\right] \\
&\quad + 96 \lim_{L,M\to\infty} \sum_{\substack{i,j=-L,-M \\ i,j\neq 0,0}}^{L,M} \left[7\frac{1}{\left\|\mathbf{r}_{i,j}^*\right\|^{16}} - 2\frac{1}{\left\|\mathbf{r}_{i,j}^*\right\|^{10}}\right] \left[\begin{array}{cccc} 3\left(x_{i,j}^*\right) & y_{i,j}^* & y_{i,j}^* & x_{i,j}^* \\ y_{i,j}^* & x_{i,j}^* & x_{i,j}^* & 3\left(y_{i,j}^*\right) \end{array}\right].
\end{aligned} \tag{B1}$$

For two particles at the position of $\mathbf{r}_{i,j}^*$ and $\mathbf{r}_{-i,-j}^*$, the distances to the origin are equal, i.e., $\left\|\mathbf{r}_{i,j}^*\right\| = \left\|\mathbf{r}_{-i,-j}^*\right\|$. From Eq. (11), it is obvious that the summation of terms $\left(x_{i,j}^*\right)^3$, $\left(x_{i,j}^*\right)^2 y_{i,j}^*$, $x_{i,j}^*\left(y_{i,j}^*\right)^2$, $\left(y_{i,j}^*\right)^3$, $x_{i,j}^*$, and $y_{i,j}^*$ for pair (i,j) and pair $(-i,-j)$ leads to zero. Thus, the whole summation in Eq. (B1) results in a zero tensor.

[1] F. F. Abraham, Phys. Rep. **80**, 340 (1981).
[2] J. M. Phillips, L. W. Bruch, and R. D. Murphy, J. Chem. Phys. **75**, 5097 (1981).
[3] M. Rovere, D. W. Heermann, and K. Binder, J. Phys.: Condens. Matter **2**, 7009 (1990).
[4] A. Z. Panagiotopoulos, Int. J. Thermophys. **15**, 1057 (1994).
[5] A. Z. Patashinski, R. Orlik, A. C. Mitus, B. A. Grzybowski, and M. A. Ratner, J. Phys. Chem. C **114**, 20749 (2010).
[6] W. Ouyang, S. Xu, and Z. Sun, Chin. Sci. Bull. **56**, 2773 (2011).

[7]A. Martinez, M. Castro, C. McCabe, and A. Gil-Villegas, J. Chem. Phys. **126**, 74707 (2007).
[8]M. Thol, G. Rutkai, A. Köster, R. Lustig, R. Span, and J. Vrabec, J. Phys. Chem. Ref. Data **45**, 23101 (2016).
[9]J. K. Johnson, J. A. Zollweg, and K. E. Gubbins, Mol. Phys. **78**, 591 (1993).
[10]J. M. Kosterlitz and D. J. Thouless, J. Phys. C: Solid State Phys. **6**, 1181 (1973).
[11]B. I. Halperin and D. R. Nelson, Phys. Rev. Lett. **41**, 121 (1978).
[12]A. P. Young, Phys. Rev. B **19**, 1855 (1979).
[13]K. J. Strandburg, Rev. Mod. Phys. **60**, 161 (1988).
[14]K. Chen, T. Kaplan, and M. Mostoller, Phys. Rev. Lett. **74**, 4019 (1995).
[15]K. Wierschem and E. Manousakis, Phys. Rev. B **83**, 214108 (2011).
[16]M. Engel, J. A. Anderson, S. C. Glotzer, M. Isobe, E. P. Bernard, and W. Krauth, Phys. Rev. E **87**, 042134 (2013).
[17]E. P. Bernard and W. Krauth, Phys. Rev. Lett. **107**, 155704 (2011).
[18]S. Jiang and K. E. Gubbins, Mol. Phys. **86**, 599 (1995).
[19]R. P. Richter, J. Lai Kee Him, B. Tessier, C. Tessier, and A. R. Brisson, Biophys. J. **89**, 3372 (2005).
[20]T. Gonen, Y. Cheng, P. Sliz, Y. Hiroaki, Y. Fujiyoshi, S. C. Harrison, and T. Walz, Nature **438**, 633 (2005).
[21]C. Mao, W. Sun, and N. C. Seeman, J. Am. Chem. Soc. **121**, 5437 (1999).
[22]Y. He, Y. Chen, H. Liu, A. E. Ribbe, and C. Mao, J. Am. Chem. Soc. **127**, 12202 (2005).
[23]W. Liu, H. Zhong, R. Wang, and N. C. Seeman, Angew. Chem. **123**, 278 (2011).
[24]K. S. Novoselov, A. K. Geim, S. V. Morozov, D. Jiang, Y. Zhang, S. V. Dubonos, I. V. Grigorieva, and A. A. Firsov, Science **306**, 666 (2004).
[25]S. Z. Butler, S. M. Hollen, L. Cao, Y. Cui, J. A. Gupta, H. R. Gutiérrez, T. F. Heinz, S. S. Hong, J. Huang, A. F. Ismach, E. Johnston-Halperin, M. Kuno, V. V. Plashnitsa, R. D. Robinson, R. S. Ruoff, S. Salahuddin, J. Shan, L. Shi, M. G. Spencer, M. Terrones, W. Windl, and J. E. Goldberger, ACS Nano **7**, 2898 (2013).
[26]S. Das, J. A. Robinson, M. Dubey, H. Terrones, and M. Terrones, Annu. Rev. Mater. Res. **45**, 1 (2015).
[27]P. Ajayan, P. Kim, and K. Banerjee, Phys. Today **69**(9), 38 (2016).
[28]D. Henderson, Mol. Phys. **34**, 301 (1977).
[29]M. R. Reddy and S. F. O'Shea, Can. J. Phys. **64**, 677 (1986).
[30]A. M. Salzberg and S. Prager, J. Chem. Phys. **38**, 2587 (1963).
[31]S. Luding, Phys. Rev. E **63**, 042201 (2001).
[32]L. Tonks, Phys. Rev. **50**, 955 (1936).
[33]A. Mulero, C. A. Galán, M. I. Parra, and F. Cuadros, *Equations of State for Hard Spheres and Hard Disks* (Springer Berlin Heidelberg, Berlin, Heidelberg, 2008).
[34]J. Kolafa and M. Rottner, Mol. Phys. **104**, 3435 (2006).
[35]D. Srivastava, E. E. Santiso, and K. E. Gubbins, Langmuir **33**, 11231 (2017).
[36]Y. Long, J. C. Palmer, B. Coasne, M. Śliwinska-Bartkowiak, and K. E. Gubbins, Phys. Chem. Chem. Phys. **13**, 17163 (2011).
[37]Y. Long, J. C. Palmer, B. Coasne, M. Śliwinska-Bartkowiak, G. Jackson, E. A. Müller, and K. E. Gubbins, J. Chem. Phys. **139**, 144701 (2013).
[38]W. G. Hoover, J. Chem. Phys. **49**, 1981 (1968).
[39]E. de Miguel and G. Jackson, J. Chem. Phys. **125**, 164109 (2006).
[40]K. S. Vasu, E. Prestat, J. Abraham, J. Dix, R. J. Kashtiban, J. Beheshtian, J. Sloan, P. Carbone, M. Neek-Amal, S. J. Haigh, A. K. Geim, and R. R. Nair, Nat. Commun. **7**, 12168 (2016).
[41]J. H. Irving and J. G. Kirkwood, J. Chem. Phys. **18**, 817 (1950).
[42]P. Schofield and J. R. Henderson, Proc. R. Soc. A **379**, 231 (1982).
[43]C. G. Gray, K. E. Gubbins, and C. G. Joslin, *Theory of Molecular Fluids 2: Applications* (Oxford University Press, 2011), pp. 928–942.
[44]A. Harasima, *Advances in Chemical Physics* (Wiley & Sons, Inc., 1958), p. 203.
[45]J. P. R. B. Walton, D. J. Tildesley, J. S. Rowlinson, and J. R. Henderson, Mol. Phys. **48**, 1357 (1983).
[46]D. J. Lee, M. M. Telo da Gama, and K. E. Gubbins, Mol. Phys. **53**, 1113 (1984).
[47]W. A. Steele, Surf. Sci. **36**, 317 (1973).
[48]T. W. Leland, P. S. Chappelear, and B. W. Gamson, AIChE J. **8**, 482 (1962).
[49]T. W. Leland, J. S. Rowlinson, and G. A. Sather, Trans. Faraday Soc. **64**, 1447 (1968).